



Published in final edited form as:

*IEEE Trans Med Imaging*. 2009 August ; 28(8): 1190–1197. doi:10.1109/TMI.2008.2011899.

## A 3D High Frequency Array Based 16 Channel Photoacoustic Microscopy System for *In Vivo* Micro-vascular Imaging

### Rachel Bitton,

University of Southern California, Los Angeles, CA 90089. She is now with the Department of Radiology, Stanford University, Stanford, CA 94305, (e-mail: rbitton@stanford.edu).

### Roger Zemp,

Washington University, St. Louis, MO 63130. He is now with the Department of Electrical and Computer Engineering, University of Alberta, Edmonton, AB Canada T6G 2V4 (zemp@ece.ualberta.ca).

### Jesse Yen,

Department of Biomedical Engineering, University of Southern California, Los Angeles, CA 90089 (email: jesseyen@usc.edu).

### L.V. Wang, and

Department of Biomedical Engineering, Washington University, St. Louis, MO 63130 (email: lhwang@biomed.wustl.edu).

### K. Kirk Shung

Department of Biomedical Engineering, University of Southern California, Los Angeles, CA 90089 (email: kkshung@usc.edu).

## Abstract

This paper discusses the design of a novel photoacoustic microscopy imaging system with promise for studying the structure of tissue microvasculature for applications in visualizing angiogenesis. A new sixteen channel analog and digital high frequency array based photoacoustic microscopy system (PAM) was developed using an Nd:YLF pumped tunable dye laser, a 30MHz piezo composite linear array transducer and a custom multi-channel receiver electronics system. Using offline delay and sum beamforming and beamsteering, phantom images were obtained from a 6 $\mu$ m carbon fiber in water at a depth of 8mm. The measured -6dB lateral and axial spatial resolution of the system was 100 $\pm$ 5 $\mu$ m and 45 $\pm$ 5 $\mu$ m, respectively. The dynamic focusing capability of the system was demonstrated by imaging a composite carbon fiber matrix through a 12.5mm imaging depth. Next, 2-D *in vivo* images were formed of vessels around 100 $\mu$ m in diameter in the human hand. 3-D *in vivo* images were also formed of micro-vessels 3mm below the surface of the skin in two Sprague Dawley rats.

## Index Terms

Photoacoustic Imaging; High Frequency Ultrasound; Transducer Array; Multichannel Receiver Electronics

## I. INTRODUCTION

Studies in oncology have shown that angiogenesis, the formation of new blood vessels within a tumor, or the growth of new blood vessels between a tumor and surrounding tissues, plays a critical role in tumor growth and metastasis of cancer [1]–[3]. Tumors need to be supplied by blood vessels, delivering oxygen and nutrients while removing metabolic waste in order to propagate. While the formation of new micro-vessels (vessels smaller than one millimeter) can be part of normal development and wound healing, it is also a key initial step in tumor progression, since tumor cells induce angiogenesis [4]. A high resolution imaging technology capable of visualizing micro-vessels would lend the ability to identify part of the early angiogenic process.

The development of novel approaches to biomedical imaging is stimulated by the manifest need for high speed, high resolution non-invasive techniques. Laser induced photoacoustic microscopy is an imaging modality based on the intrinsic optical properties of biological tissue and ultrasonic detection at high frequencies (>20MHz). Photoacoustic imaging uses short laser pulses that are absorbed in the tissue to cause acoustic pressure transients, which are detected with an ultrasonic transducer. Two factors provide exceptional motivation for the development of photoacoustic methods as a diagnostic tool in vascular imaging, the strong intrinsic optical absorption of blood, and the resolution per image depth of ultrasound.

Because of the strong scattering of light in biological tissue, optical imaging methods such as confocal microscopy and optical coherence tomography (OCT) suffer from degraded spatial resolution with increased depth. Confocal microscopy and OCT are limited to resolutions between 1–2 $\mu\text{m}$  at a 0.5mm image depth, and around 16 $\mu\text{m}$  at a 2.5mm image depth, respectively. [5]–[8]. In ultrasound, the scattering of energy is several orders of magnitude weaker than optical scattering. Therefore, energy can penetrate deeper into the tissue, providing sub-millimeter resolution at greater imaging depths compared with the optical limit [9]. For example, ultrasound backscatter microscopy (UBM) systems are capable of imaging at depths of 20mm with a 115 $\mu\text{m}$  spatial resolution, and 4mm image depths with 50 $\mu\text{m}$  spatial resolution[10][11]. Nevertheless, ultrasonic imaging suffers from reduced contrast because the detection of the backscattered signals is based on the differences of the acoustic properties in biological tissue. This presents unique position for photoacoustics, juxtaposed between two basis imaging modalities, ultrasonic and optical imaging. Photoacoustic imaging brings optical based contrast into the ultrasonic depth imaging range, attempting to capitalize on the strengths of both optical and acoustic techniques. Inherent to the technology are capabilities for functional information to be extracted [12]. By characterizing the spectrum of different optical absorbers and irradiating the sample at multiple wavelengths, photoacoustic experiments have distinguished between oxygenated and deoxygenated hemoglobin [13].

The draw to image at higher frequencies is palpable; spatial resolution improves with increased frequency. Much of the work in high frequency photoacoustic imaging has been generally confined to mechanical scans with single element transducers [14]–[17]. Methods of image reconstruction include a backprojection approach or simple time of flight measurements, as in traditional ultrasound. Backprojection techniques are similar in concept to X-ray Computed Tomography (CT) and Positron Emission Tomography (PET) scans. Various algorithms have been derived for the inverse solution to the wave equation, based on diffraction optics, to form the reconstructed image [18][19]. This method has been used to image mouse brain tissue in photoacoustic computed tomography, (PAT) [20]. In this approach a tomographic circular scan is performed using an unfocused wideband single element transducer which is scanned mechanically. High resolution PAT circular scan

images have been produced using offline backprojection reconstruction [21]. Backprojection reconstruction has also produced some trail artifacts inherent to the technique when imaging small dark absorbers such as hair fibers in tissue phantoms [17]. Unlike PAT, backward mode detection uses a focused transducer. High frequency photoacoustic images of rat micro-vessels *in vivo* have been produced by using a single element transducer, backward mode detection, and the synthetic aperture method. In one experiment, a 50MHz, single element transducer with a large numerical aperture was scanned linearly across a single axis [18][22]. There are two disadvantages to this technique; a large numerical aperture will cost imaging depth due to beam divergence past the focal zone, and the long scan time needed for mechanical scanning of the transducer. Experiments *in vivo* or *in situ* are affected by the passage of time. The condition of the live animal will change over time, and in some cases the animal may expire before the scans are complete. This is certainly a problem for functional imaging as oxygenation and blood perfusion vary after expiration.

The advantage of photoacoustic microscopy with transducer arrays over single element photoacoustic tomography is the potential to image in real time with higher frame rates. Transducer array technology facilitates fast acquisition times, as well as electronic steering and focusing of the receive beam. Arrays provide parallel photoacoustic signal detection through adjacent transducer elements which each possess their own electrical connections. Although array technology is common in frequencies below 20 MHz, high frequency transducer arrays pose challenges both in the fabrication process, performance demands, and parallel multi-channel electronic system design [23]. The frequency of the photoacoustic echoes that are generated are dependent on the size of the vessel or absorber, causing the bandwidth performance of the transducer to be of particular importance. For high frequency arrays, the complexity of high speed electronic design increases as channel number increases. Proper noise suppression, isolation, sampling, and critical timing restraints set the boundaries for high frequency photoacoustic systems. Until now, most of the work in photoacoustic imaging has been executed using commercially available components either in single element transducer/single channel systems using oscilloscopes, or using lower frequency arrays with commercial ultrasound systems [16][17][24]. Our aim was to create a novel multi-channel high resolution photoacoustic microscopy system to visualize micro-vascular structures in rats. In this paper we present a prototype 16 channel receiver system which was developed to accommodate a custom made high frequency transducer array.

The photoacoustic microscopy receiver system uses multi-channel parallel signal processing, in backward mode detection, to acquire the raw data from each element in the transducer array. This method is especially useful and differs from current high frequency ultrasound linear array systems in which active channels are beamformed via hardware, followed by transfer of the beamformed data to a PC [25]. Transmitting and capturing the raw RF (Radio Frequency) data from all active channels provides the distinctive ability to access RF data from each individual element, allowing the most flexibility for beamforming, and image reconstruction.

## II. THEORY

Photoacoustic imaging has its physical basis in a phenomenon called the optoacoustic, or photoacoustic effect. This effect can be observed in a variety of media, including biological tissue, wherever pulsed electromagnetic energy can be absorbed [24]. Under conditions of thermal and stress confinement, short laser pulses will induce acoustic waves most efficiently. As incident laser light in the visible spectrum interacts with tissue, it is either absorbed by local chromophores, or scattered in various extents depending on the inherent optical properties of the tissue [27]. The photoacoustic effect occurs when the pulsed light energy is absorbed locally in biological tissue, and a small rapid temperature rise in the

medium causes thermoelastic expansion. This expansion produces pressure transients, which propagate as acoustic waves throughout the tissue omni-directionally [28]. The initial pressure generated,  $p_i$  is related to the spatial portion of heating function  $H(\mathbf{r})$  at position  $\mathbf{r}$ , and the Grüneisen parameter ( $\Gamma$ ). Initial pressure can then be written

$$p_i(\mathbf{r}) = \Gamma \cdot H(\mathbf{r}) \quad (1)$$

In this form,  $H(\mathbf{r}) = \mu_a(\mathbf{r}) F(\mathbf{r})$ , where  $F$  is the local fluence in ( $\text{J}/\text{m}^2$ ), determined by the incident light as well as the scattering and absorption parameters  $\mu_s$  and  $\mu_a$ , respectively [29]. Subsequent pressure generated at given time and position incorporates the initial pressure and obeys the common form of the time retarded wave equation. Thus, the pressure profile of the generated photoacoustic echo is based on the optical properties of the target in the media, and does not necessarily mimic the profile of the laser pulse itself.

Tissue absorbs light differently at specific wavelengths, conditional to the optical properties of the medium. Photoacoustic imaging is especially well suited for vascular imaging since in the visible spectrum, light absorption in sub-dermal tissue is principally due to the dominant chromophores oxy- and deoxy-hemoglobin [30].

As a result of the high optical scattering of light in tissue, photoacoustic imaging does not focus the transmit (light) beam as in ultrasonic imaging techniques. Rather, photoacoustic imaging utilizes the multiple scattering effects to its advantage. While optical based methods rely on the signals of only singly backscattered photons [8], which effect image speckle and limit penetration depth, the cumulative effect of multiple scattering aids to a better perfusion of energy, and maximizes irradiation homogeneity of the tissue. Photoacoustic signals are generated from the region of interest within the tissue. Consequently, they are subject to only one-way, rather than round-trip, ultrasonic image quality degrading aberrations. Additionally, the echo wait time is approximately half that of ultrasound. For single wavelength excitation, it is possible that a multi-channel photoacoustic imaging system with the proper parameters would be capable of constructing *in-vivo* images in real time with only one nanosecond duration laser pulse.

The axial and lateral resolution of a photoacoustic image is determined by the generated acoustic echo and transducer properties. The beam width of the active transducers in the array scan determines the theoretical lateral spatial resolution of the system. It can be related proportionally to the transducer wavelength by

$$\text{LR} \approx f_{\#} \lambda \quad (2)$$

where the f-number,  $f_{\#}$  is the ratio of focal distance to aperture dimension.

### III. MATERIALS AND METHODS

#### A. System Design

The photoacoustic microscopy system is comprised of three main components: An Nd:YLF laser source used to irradiate the tissue and induce photoacoustic waves, a 48 element piezo composite transducer array which receives the photoacoustic waves, and a custom 16 channel parallel receive electronic system. The photoacoustic electronic system controls the laser operations, and processes and digitizes the data from the transducer array (Figure 1). In the experimental setup both the transducer array and optical fiber are mounted on a 3D translation stage, and then lowered into a water tank. The process initiates when a TTL signal from the photoacoustic system motherboard triggers the laser pulse to irradiate the sample through the optical fiber positioned obliquely to the sample and array. After each

laser pulse, the 16 element sub-aperture is processed through the analog and digital boards, and then stored to the PC. To fully sample the 48 element array, the laser fires three times for each image acquisition. Algorithms were written for the PAM system in Labview and Matlab. They provide a user interface, and delay and sum photoacoustic image reconstruction.

The laser setup includes a diode-pumped Nd:YLF Q-switched laser (INNOSLAB Edgewave, Germany) and a tunable dye laser (Cobra, Sirah Laser, Germany). The Q-switch is an externally triggered attenuator which modulates the Q factor of the optical resonator cavity, producing 6.5ns pulses at 14mJ when deactivated. The dye laser is used to tune the light to 598nm, and produced 2mJ per pulse. The light is then coupled by a beam shaper and microscope objective into a 600 $\mu$ m optical fiber which delivered a per pulse energy of 0.8mJ. Since the area of illumination on the skin surface was about 2 $\times$ 4mm, the energy fluence was estimated as 10mJ/cm<sup>2</sup> (ANSI maximum = 20mJ/cm<sup>2</sup>).

The linear transducer array used is constructed of a 2-2 piezo composite material measuring ~4.8mm $\times$ 2mm in the azimuth and elevation directions, respectively. It contains 48 rectangular elements centered at 30MHz, and is used in receive mode only. The array elements bear a 2 $\lambda$  (100 $\mu$ m) pitch, and use a lens to form an elevational focal depth of 8mm [29]. The simulated one way -6dB fractional bandwidth (Full Width Half Maximum) of the array is 70%. The receive electronics were developed to include signal processing and data transfer in two separate stages; analog and digital (Figure 2). All 48 elements are connected to receive circuits including preamplification. They are then multiplexed down to create 16 active channels which pass through filtering, fixed and variable gain stages. The 16 analog channels are then converted to 16 digital channels using 8 channelboards which digitize two channels each and store in temporary memory before transfer to the computer.

The first stage is comprised of the front end receive and signal processing electronics (Blocks 1 and 2, Figure 2). The array elements interface with the PAM system through RG-174 shielded RF cables and SMA connectors (Figure 3a). On the front end receive system; each of the 48 elements contains a fixed, ultra low noise, 18dB, pre-amplification stage (MAX4107, Maxim/Dallas Semiconductor). Four-to-one multiplexers are used to select between elements (AD8184, Analog Devices), forming 16 active channels. Following channel formation, a 4<sup>th</sup> order Butterworth band pass filter is used to remove spurious signals with frequencies out of the desired transducer response. The filter was designed to have a wide response and sharp cutoff so that it can also double as an anti-aliasing filter before analog to digital conversion stages. The signal is then amplified by low noise, dual variable gain amplifiers (VGA) providing a 0–40dB gain range (AD8332, Analog Devices). The differential outputs of the VGA are converted back to single ended signals through transformers (T1 6T, Minicircuits), which also provide signal isolation. A final fixed gain stage boosts the signal another 20dB. The measured system receiver gain provides a selectable range from 33dB–73dB.

The second stage of the receiver system digitizes, provides the timing network for the system, and controls data transfer through a motherboard-channelboard scheme (similar to the design within a PC) (Block 3, Figure 2). The digital system supplies the master triggering, providing clock synchronized triggers for the laser, the receive electronics, and the PC data transfer card. The laser is triggered first at a 5Hz repetition rate. After a programmable delay, the acquisition is triggered to account for the latency between the laser trigger and the optical delivery. The 16 channel group raw data is acquired in less than 11ms after each laser pulse. Then, handshaking control and clock signals are provided to transfer data using a PCI based digital NI-6534 card (National Instruments). Each complete image frame required 3 laser shots.

The high frequency array imposed challenges on electronic component performance and on system design. High speed considerations for multi-channel systems such as bus topology, impedance matching, and clock synchronization influenced both schematic design and manual board layout. To ensure proper timing synchronization of multiple channels, all control and clock signals are based on divisions of a single 100MHz oscillator. The digital system contains 9 channelboards that plug into a motherboard through high speed connectors (Q-Series, Samtec) (Figure 3b). Each channelboard receives two analog channels, and contains two 8-bit, 100MHz, analog to digital converters (AD9054, Analog Devices), one 16-bit temporary memory storage FIFO with 1K depth, providing an imaging depth of about 15mm (SN74V225, Texas Instruments). Each FIFO is shared between two channels, and a line driver on each channelboard selects a particular board for transfer. The first eight channelboards digitize each group of 16 elements from the array, while the ninth channel is dedicated to laser energy measurements, provided by a photodiode. The motherboard provides the 16-bit data bus; interconnect to channelboards and to the PC, as well as the clock distribution network. Using the 16-bit NI-6534 running at 12.5MHz, digital data is transferred to the PC at a rate of 25MB/s for each channelboard.

## B. Image Reconstruction

Images are created using offline delay and sum beamforming and beamsteering. To calculate a single image A-scan line the RF data is used from all 48 elements, rather than the 16 element subaperture. This establishes a narrow beam focus and thus, a more desirable lateral spatial resolution. To form the beam and steer the beam, delays are applied to each element using a simple geometric model. Assuming a distance  $d$  to the target point at a lateral distance  $x_n$  and angle  $\varphi$  from the element in question (relative to the center element reference), the time delay  $\Delta\tau_n$  for element number  $n$  can be written as

$$\Delta\tau_n(d, \varphi) = \frac{\sqrt{(x_n + d \sin \varphi)^2 + d^2 \cos^2 \varphi} - d}{c_a} \quad (3)$$

where  $c_a$  is the sound velocity through the medium. This is identical to conventional ultrasound time delay calculations except that the one way trip distance for received echoes is accounted for applying  $c_a t = d$ .

During beamformation, coherence factor weighting was applied to the phantom image data. This technique aids to reduce focusing errors resulting from sound velocity inhomogeneities, as well as steering errors. The coherence factor equation is given by

$$CF(t, \varphi_s) = \frac{\left| \sum_{n=0}^{N-1} S(n, t - \Delta\tau_n(d, \varphi_s)) \right|^2}{N \sum_{n=0}^{N-1} |S(n, t - \Delta\tau_n(d, \varphi_s))|^2} \quad (4)$$

where  $N$  is the number of elements and  $S(n, t - \Delta\tau_n(d, \varphi_s))$  is the channel data for a given scan line angle  $\varphi_s$ , after the time delays for steering and focusing have been applied [32].

## C. Experimental Setup

A spectrum analyzer was used to illustrate the frequency response of the entire receive system. To demonstrate functionality and to characterize system performance, phantom images were obtained. The phantom consisted of a  $6\mu\text{m}$  carbon fiber in water, imaged at the transducer array focal depth of 8mm.

*In vivo* rat images were obtained using the same experimental setup as the phantoms for two different rats. A Sprague Dawley rat was prepared by depilating a section on the back to reduce excessive signal loss from the fur and then fixing the animal position below the water tank. Small subcutaneous vessels were imaged at the transducer focus (6mm – 10mm), and a few millimeters below the surface of the skin. After imaging, the animal was sacrificed, and the area imaged was excised for comparison and verification of vessel structure.

## IV. RESULTS

### A. System Characterization

To assess the bandwidth of the assembled receiver system, the frequency response was measured between the front end (transducer element input stage) and the final RF output stage using a spectrum analyzer (E4401B, Agilent). The passband of the measured receiver response encompasses the -6dB one way transducer response and additionally displays a wider band performance (Figure 4). The transducer array bandwidth dictates the bandwidth for following stages. However, the PAM receiver allows flexibility if the system is later paired with a high frequency array of greater fractional bandwidth, which is currently under development. A 1.2dB ripple in the measured frequency response is observed due filter trade off relationships that exist between bandwidth, roll-off, and complexity.

To characterize the sensitivity of the front end, the minimum detectable signal was measured. A function generator providing a 30MHz sine wave was connected to a variable gain attenuator and then fed into the front end of the receive electronics. The signal was measured at two subsequent test points, and the minimum detectable signal was calculated given the known input signal and attenuation. Test point 1 was measured using an oscilloscope at the output of the analog signal processing board. Test point 2 was measured after the digital boards, using the RF signal at the PC display stage, to quantify the effect of digital switching noise to the system. The minimum detectable signal was 316 $\mu$ V and 500 $\mu$ V, approximating the noise floor at test points 1 and 2, respectively. Using the KLM model, the minimum detectable signal of 500 $\mu$ V at 30MHz corresponds to an estimated minimum detectable transducer pressure of  $\sim 0.51$  kPa.

Spatial resolution information was extracted by imaging a single 6 $\mu$ m carbon fiber in water and projecting the image data onto one axis to construct the line spread function, showing the signal strength vs. spatial distance (Figure 5). Both axial and lateral resolutions were based on the -6dB width of the carbon fiber in each image direction. The lateral and axial spatial resolution of the system at the transducer focal point was measured as  $100\pm 5\mu$ m and  $45\pm 5\mu$ m, respectively. We have previously reported an axial resolution of 25 $\mu$ m with a similar system [33]. In that study, instead of using the -6dB width, the axial resolution was measured by superimposing the signal from a single carbon fiber with the signal from the same fiber translated vertically, and examining the envelope. The separation distance between two distinguishable peaks was used as the axial resolution figure of merit, 25 $\mu$ m.

To express the dynamic focusing capability of PAM, a composite image was constructed by imaging the 6 $\mu$ m carbon fiber in evenly spaced positions. The images from each carbon fiber represented a matrix of target locations and were combined together to create a composite image. The carbon fiber matrix is made up of 5 rows with a 1mm separation in depth by 9 columns with 1.1016mm lateral separations (Figure 6). To obtain this data set, the optical fiber is fixed relative to a single carbon fiber, while the transducer position is moved. This ensures a more uniform illumination of the target regardless of the matrix position. The data was taken with 598nm wavelength light in water. The two dead elements of the array may explain a slight variation in sensitivity (upper right corner); however, it is shown that the targets are well focused throughout the region of interest.

## B. Images

In vivo images B-scans were obtained from the lower portion of a human hand using a wavelength of 568nm and a laser fluence of 7mJ/cm<sup>2</sup>. A number of bright signals from microvessels less than 100µm in diameter can be seen in the center of the image (Figure 7).

This progression led to 3D photoacoustic rat microvessel images *in vivo*. Spaced at 0.005 inch (0.127mm) intervals in the elevation direction (perpendicular to the B-scan plane), 100 B-scans were acquired along the image plane using a 3 axis translation stage for the transducer array. With 10mJ/cm<sup>2</sup> incident fluence at 598nm and an averaging index of 16, subcutaneous vessels were imaged at depths of 3 mm below the skin's surface (in the 8mm focal zone) in two Sprague Dawley rats (Figure 8). Offline image reconstruction was executed in ~1 min. Because of the dense vasculature within the tissue, the images shown are reconstructed from a small truncated portion of the data in the depth direction, in order visualize the overlaid vessel structures at a given depth. Microvessels of different diameters and vessel bifurcation can be identified at varying depths within the truncated range. These vessels were not visible from the skin's surface. The animals were then sacrificed and portions of skin excised to verify vessel structures.

## I. DISCUSSION

The noise visible in the 3D image could be related to the 3D reconstruction static thresholding techniques were used to form the boundaries of the vessel structures as 3D surfaces. A more robust approach might include a dynamic thresholding technique which could refine the surface boundary threshold for areas outside of the focal zone of the transducer. Additionally, system noise contributions can be related to the lack of shielding of the electronic system. The RF cables used for each transducer element carry small signals that travel from the array to the connector box, and then to the front end of the board. These cables are bundled closely and can contribute to signal loss and potential crosstalk. Future array designs could integrate lines into a single shielded RF connector which plugs directly into the PCB board.

The greatest improvement in SNR may be made in optimization of the light delivery technique. These experiments were conducted with no more than half the laser fluence limit (20mJ/cm<sup>2</sup>). A more efficient light delivery scheme could improve the amount of laser energy delivered to the tissue, yielding greater photoacoustic signal strength. Other approaches to photoacoustic sensitivity enhancement are being investigated by the introduction of exogenous contrast agents, such as gold nanoshells [34].

In Fig. 8(c), the upper vessel could not be compared to the photo since that portion of the tissue was not recovered during the skin excising process. Some vessels are also disconnected by a missing slice which may have been caused by missing data sets, motion artifacts, or could possibly be improved by decreasing the slice intervals at which the scans are taken. It is also important to mention that vessels of larger diameters will produce photoacoustic echoes of lower frequency compared with those of smaller diameters. The large vessel low frequency echoes may be difficult to resolve if they are outside of the transducer bandwidth.

A future development for the system is to image in real time by increasing the pulse repetition frequency of the laser (up to 1KHz), increasing the acquisition transfer speed through hardware, and increasing the speed of the processor which executes beamformation and running the image reconstruction algorithm in C programming, rather than Matlab. The limitation of time between laser shots (analogous to pulse repetition frequency, PRF) is the execution of the Labview program. The Labview program which controls the FIFO to PC

transfer creates a data transfer bottleneck as it is not based on a real-time platform, the timing is non-deterministic, and may produce PRF fluctuations in the ms error margin. Although the diode-pumped Nd:YLF laser permits triggering at arbitrary rates unlike flashlamp-pumped lasers, a faster deterministic PRF could provide more uniform energy deposition between laser pulses. The transfer speed control timing issue can be overcome through hardware by providing control signals from a dedicated processor or CPLD. This would alleviate the problem, since both the sampling of RF data (100MHz) and each 16 channel PC transfer (12.5MHz) on this PAM system are fast enough for 1KHz pulse repetition rates and real time imaging. This would eliminate the Labview barrier, delivering completely deterministic control between laser events and provide data fast enough for 16 channel real time PAM imaging.

## II. CONCLUSION

A new 30MHz array based photoacoustic imaging system was developed in which raw RF photoacoustic data is accessible for all 48 elements and images were formed after 3 laser pulses. The 16 channel photoacoustic receive system was fabricated and characterized, then used to create phantom images of 6 $\mu$ m carbon fibers in water. The -6dB axial and lateral spatial resolution of the system was measured as 45 $\pm$ 5 $\mu$ m and 100 $\pm$ 5 $\mu$ m, respectively. The dynamic focusing capability was demonstrated through a 12.5 mm depth using a composite image of a carbon fiber matrix. 2-D *in vivo* images were formed of micro-vessel structures in the human hand. 3-D *in vivo* images were also formed of micro-vessels below the surface of the skin in two Sprague Dawley rats.

Photoacoustic microscopy is a non-ionizing modality with much room for growth, holding great promise for medical imaging. Some of the most attractive qualities include a scalable resolution and imaging depth dependent upon the ultrasonic transducer frequency, no speckle artifacts, high contrast, and the extension towards real time imaging. To compensate for the limitations of light scattering in deeper tissues and to provide images based on the acoustic and optical properties of the medium, both conventional ultrasound images and photoacoustic images can be used for comparison, and to provide two different types of contrast. A bimodal imaging system could produce a simultaneous display of photoacoustic and pure ultrasonic images acquired from the same cross sections of tissue, supplying an anatomical reference for the photoacoustic signals. Furthermore, these images could be constructed by utilizing the same transducer array for both modalities, offering added diagnostic value without the need for two separate systems.

The high frequency PAM array system presented in this paper offers a new perspective on the capabilities of photoacoustic imaging. High resolution photoacoustic images can have applications in oncology by tracking the important vascular structures associated with angiogenesis.

## Acknowledgments

Authors would like to acknowledge J. M. Cannata for his work in the design and fabrication of the high frequency transducer array.

This work was supported in part by the National Institute of Health under Grants R01 EB000712 and P41-EB2182.

## REFERENCES

1. Folkman J. Angiogenesis in cancer, vascular, rheumatoid and other disease. *Nature Medicine*. 1995 Jan.;27–31.

2. Yancopoulos GD, Davis S, Gale NW, Rudge JS, Weigand SJ, Holash J. Vascular-specific growth factors and blood vessel formation. *Nature*. 2000; vol. 407:242–248. [PubMed: 11001067]
3. Papetti M, Herman IM. Mechanisms of normal and tumor-derived angiogenesis. *American Journal of Physiology: Cell Physiology*. 2002; vol. 282(Issue 5):C947–C970. [PubMed: 11940508]
4. Liu J, Razani B, Tang S, Terman B, Ware JA, Lisanti M. Angiogenesis Activators and Inhibitors Differentially Regulate Caveolin-1 Expression and Caveolae Formation in Vascular Endothelial Cells. *J. of Biol. Chemistry*. 1999; vol. 274(Issue 22):15781–15785.
5. Kempe M, Rudolph W, Welsch A. Comparative study of confocal and heterodyne microscopy for imaging through scattering media. *Journal of the Optical Society of America A: Optics and Image Science*. 1996; vol. 13:46–52.
6. Singh A, Gopinathan KP. Confocal microscopy – a powerful technique for biological research. *Current Science*. 1998; vol. 74:841–851.
7. Wang RK, Jacques SL, Ma Z, Hurst S, Hanson SR, Gruber A. Three dimensional optical angiography. *Optics Express*. 2007; vol. 15:4083–4097. [PubMed: 19532651]
8. Huang D, Swanson EA, Lin CP, Schuman JS, Stinson WG, Chang W, Hee MR, Flotte T, Gregory K, Puliafito CA, Fujimoto JG. Optical coherence tomography. *Science*. 1991; vol. 254:1178–1181. [PubMed: 1957169]
9. Duck, FA. *Physical Properties of Tissue*. London: Academic Press; 1990.
10. Zhou YQ, Foster FS, Nieman B, Davidson L, Chen XJ, Henkelman RM. Comprehensive transthoracic cardiac imaging in mice using ultrasound biomicroscopy with anatomical confirmation by magnetic resonance imaging. *Physiological Genomics*. 2004; vol. 18:232–244. [PubMed: 15114000]
11. Sun L, Richard WD, Cannata JM, Fang CC, Johnson J, Yen JT, Shung KK. A high-frame rate high-frequency ultrasonic system for cardiac imaging in mice. *IEEE Trans on Ultrasonics, Ferroelectrics, and Frequency Control*. 2007; vol. 54:1648–1655.
12. Zhang HF, Maslov K, Stoica G, Wang L-H. Functional photoacoustic microscopy for high-resolution and noninvasive *in vivo* imaging. *Nature Biotechnology*. 2006; vol. 24:848–851.
13. Wang X, Xie X, Ku G, Stoica G, Wang L-H. Non-invasive imaging of hemoglobin concentration and oxygenation in the rat brain using high-resolution photoacoustic tomography. *Journal of Biomedical Optics*. 2006 Mar-Apr; vol. 11(2):024015. [PubMed: 16674205]
14. Karabutov AA, Savateeva E, Podymova N, Oreavsky A. Backward mode detection of laser induced wide band ultrasonic transients with photoacoustic transducer. *J. of Applied Physics*. 2000; vol. 87:2003–2014.
15. Su Y, Zhang F, Xu K, Yao J, Wang R. A photoacoustic tomography system for imaging of biological tissues. *Journal of Physics D: Applied Physics*. 2005; vol. 38:2640–2644.
16. Maslov K, Stoica G, Wang LH. *In Vivo* dark-field reflection mode photoacoustic microscopy. *Optics Letters*. 2005; vol. 30:625–627. [PubMed: 15791997]
17. Sethuraman S, Aglyamov SR, Amirian JH, Smalling RW, Emelianov SY. Intravascular photoacoustic imaging using an IVUS imaging catheter. *IEEE Trans. on Ultrasonics Ferroelectrics and Frequency Control*. 2007; vol. 54:978–986.
18. Xu M, Wang L. Universal back projection algorithm for photoacoustic computed tomography. *Physical Review*. 2005; vol. 71:1–7.
19. Kostli K, Frenz M, Bebie H, Weber H. Temporal backward projection of photoacoustic transients using Fourier transform methods. *Physics in Medicine and Biology*. 2001; vol. 46:1863–1872. [PubMed: 11474930]
20. Wang X, Pang Y, Ku G, Xie X, Stoica G, Wang L-H. Noninvasive laser-induced photoacoustic tomography for structural and functional imaging of the brain *in vivo*. *Nature Biotechnology*. 2003 Jul; vol. 21(7):803–806.
21. Xu M, Wang LH. Time-domain reconstruction algorithms and numerical simulations for thermoacoustic tomography in various geometries. *IEEE Transactions in Biomedical Engineering*. 2003; vol. 50:1086.
22. Wang LV, Li ML, Zhang HF, Maslov K, Stoica G. High resolution photoacoustic tomography *in vivo*. *Proceedings of the 2006 IEEE International Symposium on Biomedical Imaging: Macro to Nano*. 2006:1204–1207.

23. Cannata J, Shung KK. A comparison of model and experiment for a high frequency (35 MHz) ultrasonic array. Proceedings of the 2003 IEEE Ultrasonics Symposium. 2003:1658–1662.
24. Niederhauser JJ, Jaeger M, Lemor R, Weber P, Frenz M. Combined ultrasound and optoacoustic system for real-time high contrast vascular imaging *in vivo*. IEEE Trans. on Medical Imaging. 2005; vol. 24:436–440.
25. Hu CH, Xu XC, Cannata JM, Yen JT, Shung KK. Development of a Real-Time, High-Frequency Ultrasound Digital Beamformer for High-Frequency Linear Array Transducers. IEEE Trans. on Ultrasonics Ferroelectrics and Frequency Control. 2006; vol. 53:317–323.
26. McQueen D. Acoustical theory of the photoacoustic effect in gaseous and liquid media. Journal of Applied Physics. 1979; vol. 12:1673–1678.
27. Cheong W-F, Prah SA, Welch AJ. A review of the optical properties of biological tissues. IEEE J. Quantum Electron. 1990; vol. 26:2166–2185.
28. Gusev, VE.; Karabutov, AA. Laser Optoacoustics. New York: AIP Press; 1993.
29. Cox BT, Arridge SR, Köstli KP, Beard PC. Quantitative photoacoustic imaging: fitting a model of light transport to the initial pressure distribution. Proc. SPIE. 2005; vol. 5697:49–55.
30. Xu H, Patterson M. Determination of the optical properties of tissue-simulating phantoms from interstitial frequency domain measurements of relative fluence and phase difference. Optics Express. 2006; vol. 14:6485–6501. [PubMed: 19516827]
31. Cannata JM, Williams J, Zhou Q, Ritter T, Shung KK. Development of a 35 MHz piezo-composite ultrasound array for medical imaging. IEEE Transactions on Ultrasonics Ferroelectrics and Frequency Control. 2006; vol. 53:224–236.
32. Liao C-K, Li M-L, Li P-C. Optoacoustic imaging with synthetic aperture focusing and coherence weighting. Optics Letters. 2004; vol. 29:2506–2508. [PubMed: 15584276]
33. Zemp RJ, Bitton R, Li M-L, Shung KK, Stoica G, Wang LV. Photoacoustic imaging of the microvasculature with a high-frequency ultrasound array transducer. J. of Biomedical Optics. 2007; vol. 12(1)
34. Xiang L, Da X, Gu H, Yang D, Zeng L, Yang S. Gold nanoshell-based photoacoustic imaging application in biomedicine. Proceedings of the 2006 IEEE International Symposium on Biophotonics, Nanophotonics and Metamaterials. 2006:76–79.

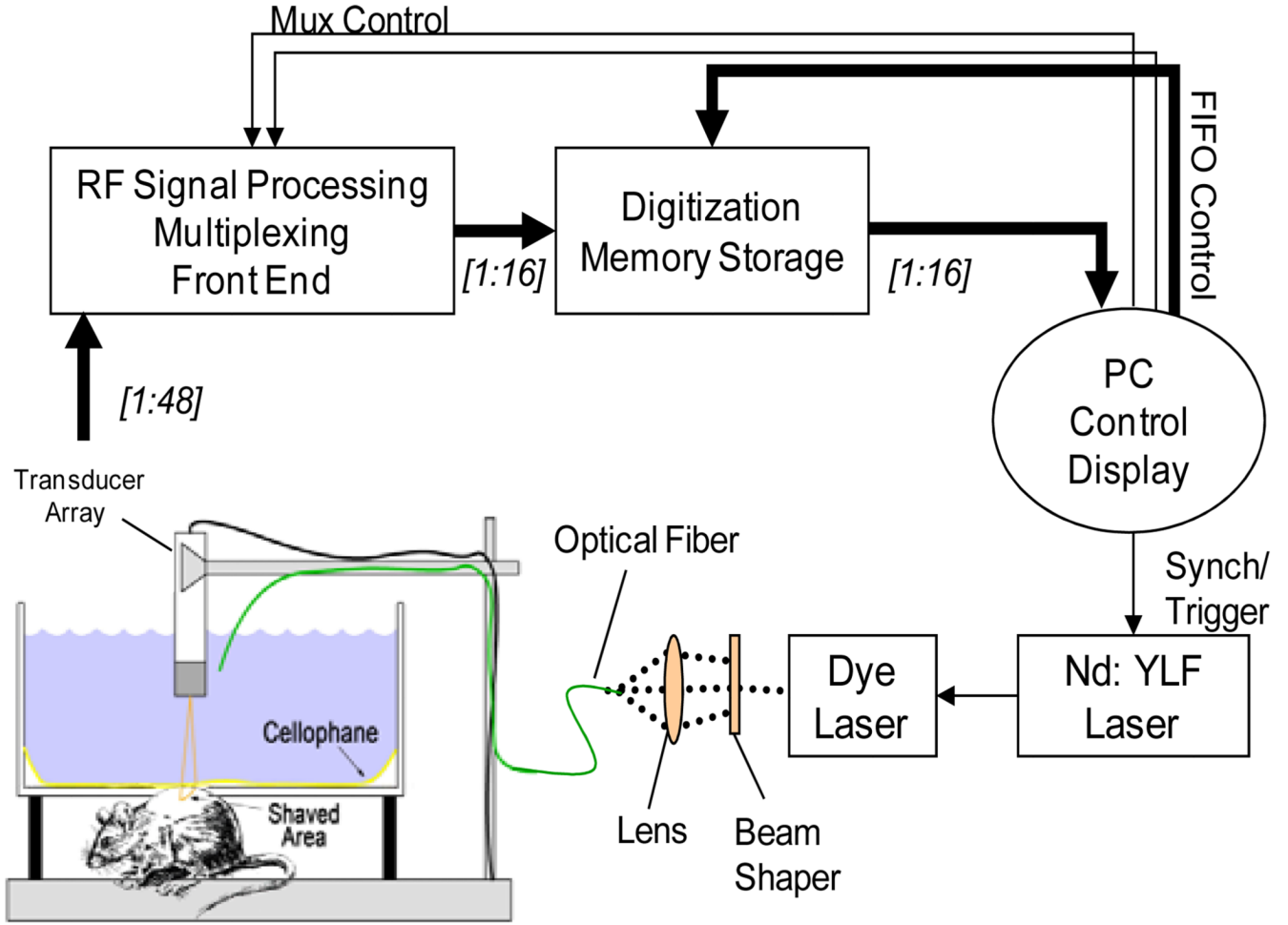


**Fig. 1.** PAM system setup. The laser is triggered and coupled by a lens to an optical fiber to illuminate the sample. Photoacoustic waves are received through 48 elements in the transducer array. For each laser event, the system provides the receive front end, filtering and amplification stages, and transfers raw data from 16 elements of the array. The laser fires 3 times in order to collect the photoacoustic data from all 48 elements in the array.

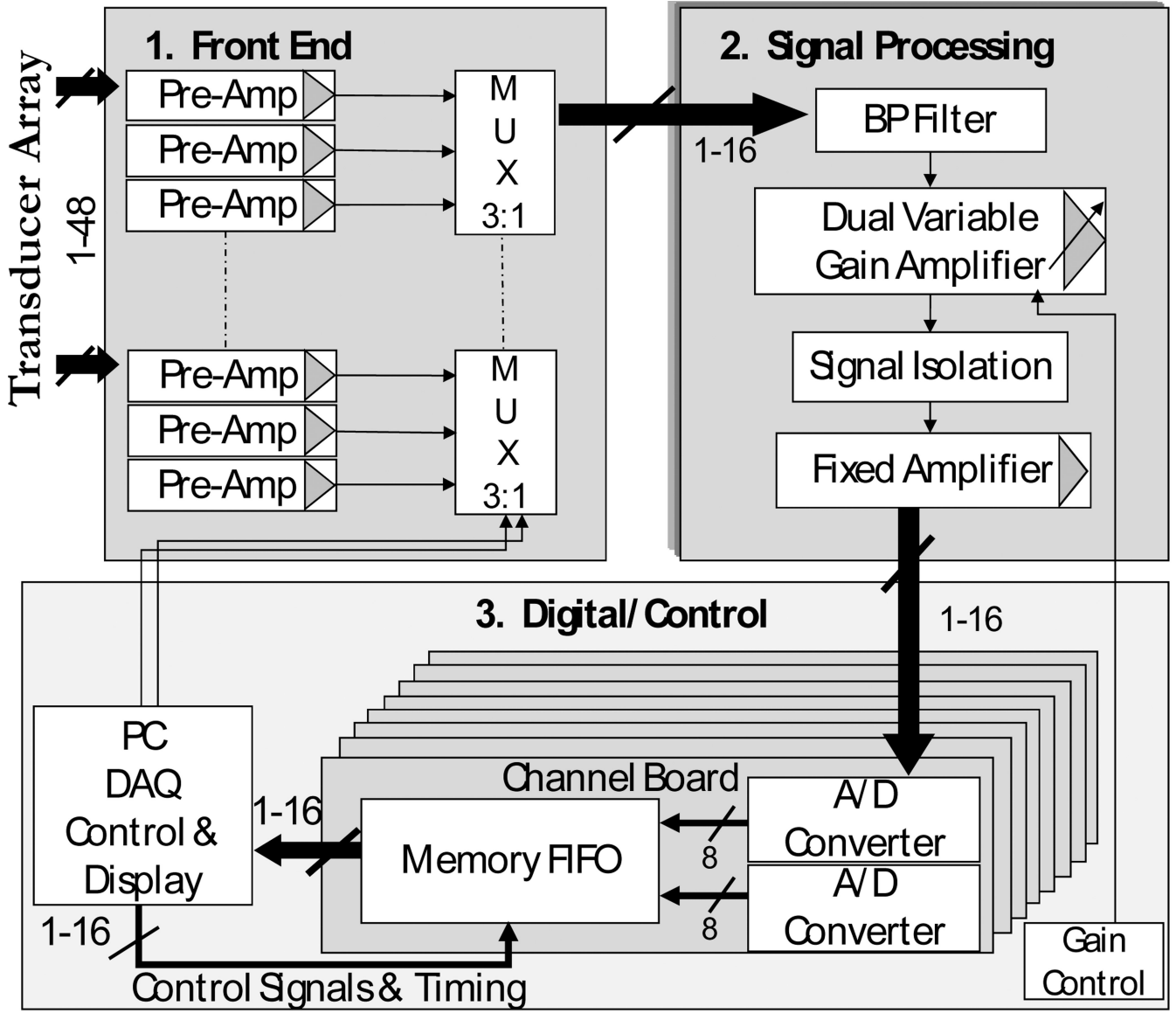
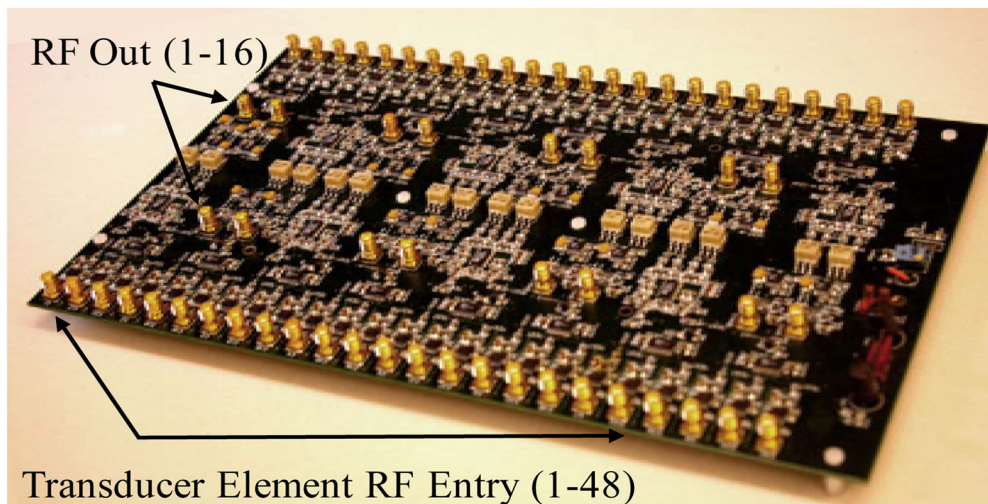
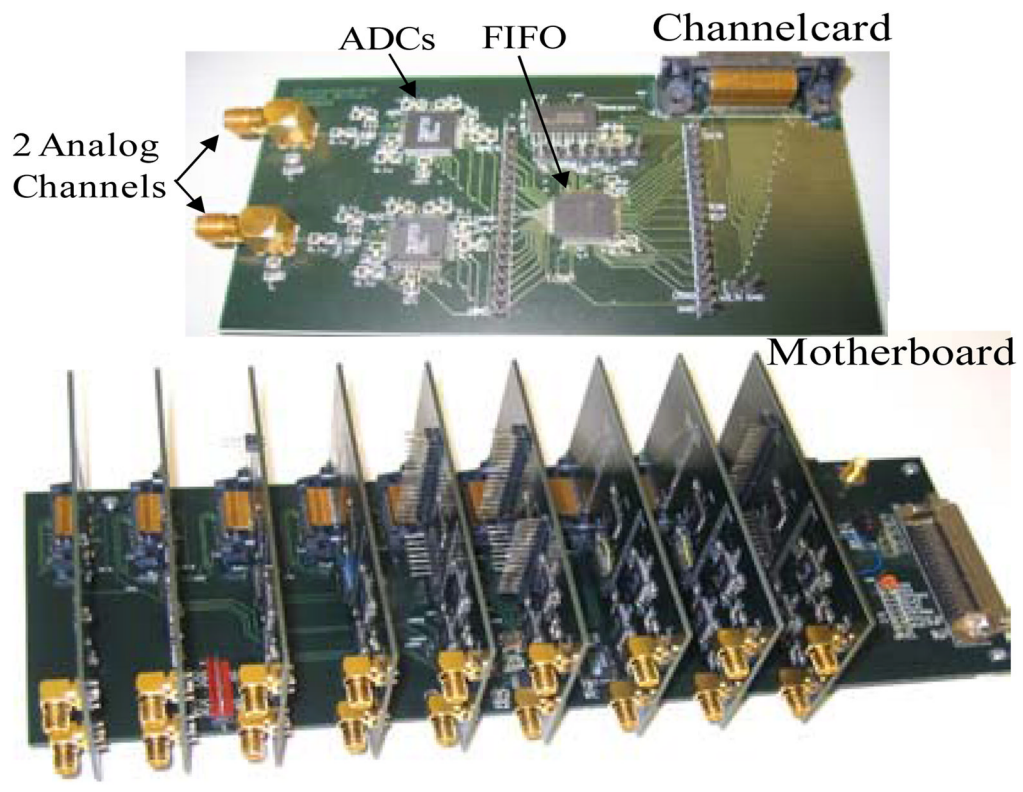


**Fig. 2.** PAM receive system architecture. The transducer array elements all receive preamplification before being multiplexed. The channels then pass through filtering, variable, and fixed gain stages before A/D conversion. 8 channel cards accommodating 2 channels each send digital data to the computer via the PCI bus.



a) Transducer Element RF Entry (1-48)



b)

**Fig. 3.** Photo of the fabricated a) 16 channel analog receiver board implemented on a 4 layer PCB (Printed Circuit Board) and b) digital PAM system with motherboard and channelcards implemented on a 6 layer PCB.

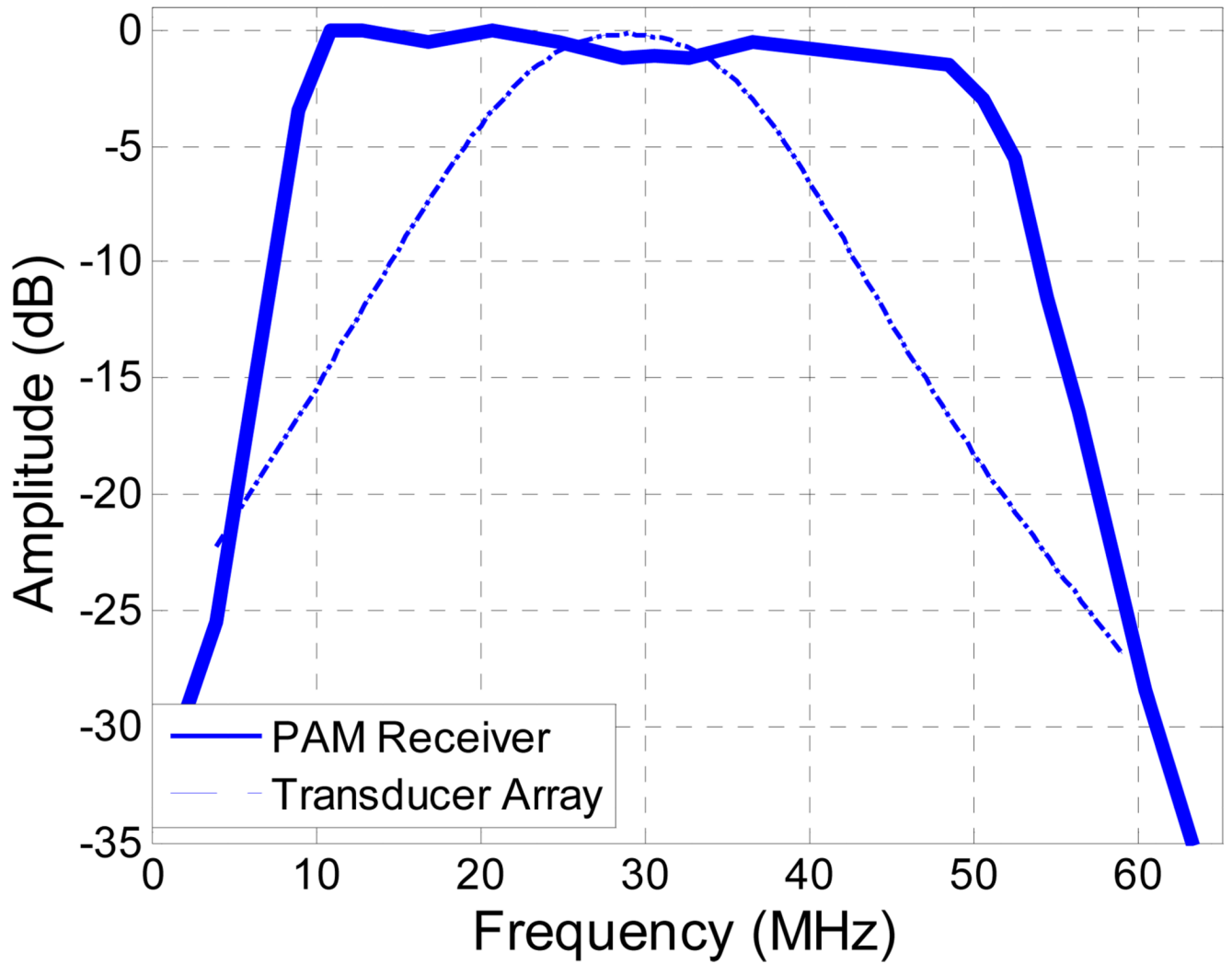


**Fig. 4.**  
PAM receiver frequency response and 30MHz transducer array frequency response.

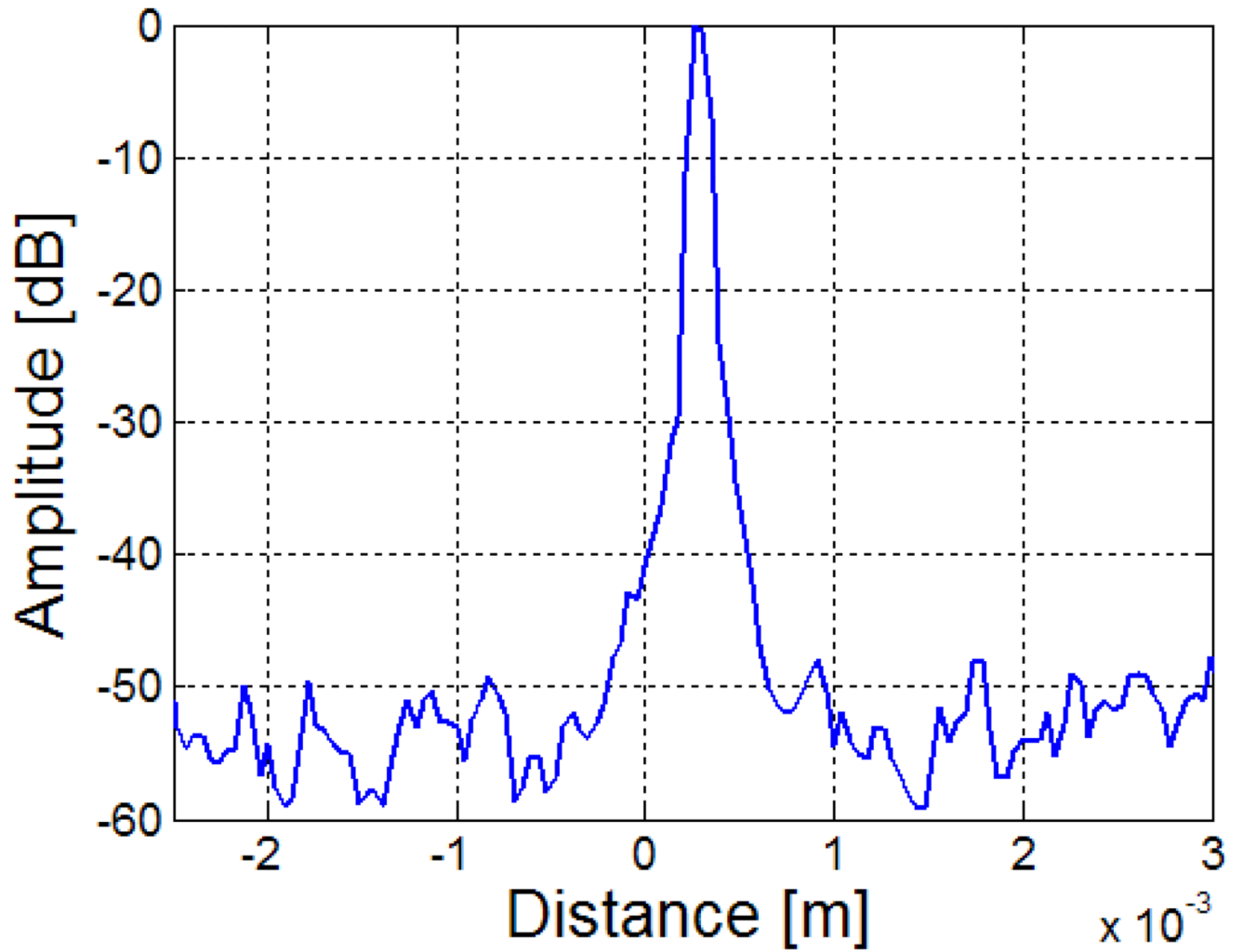
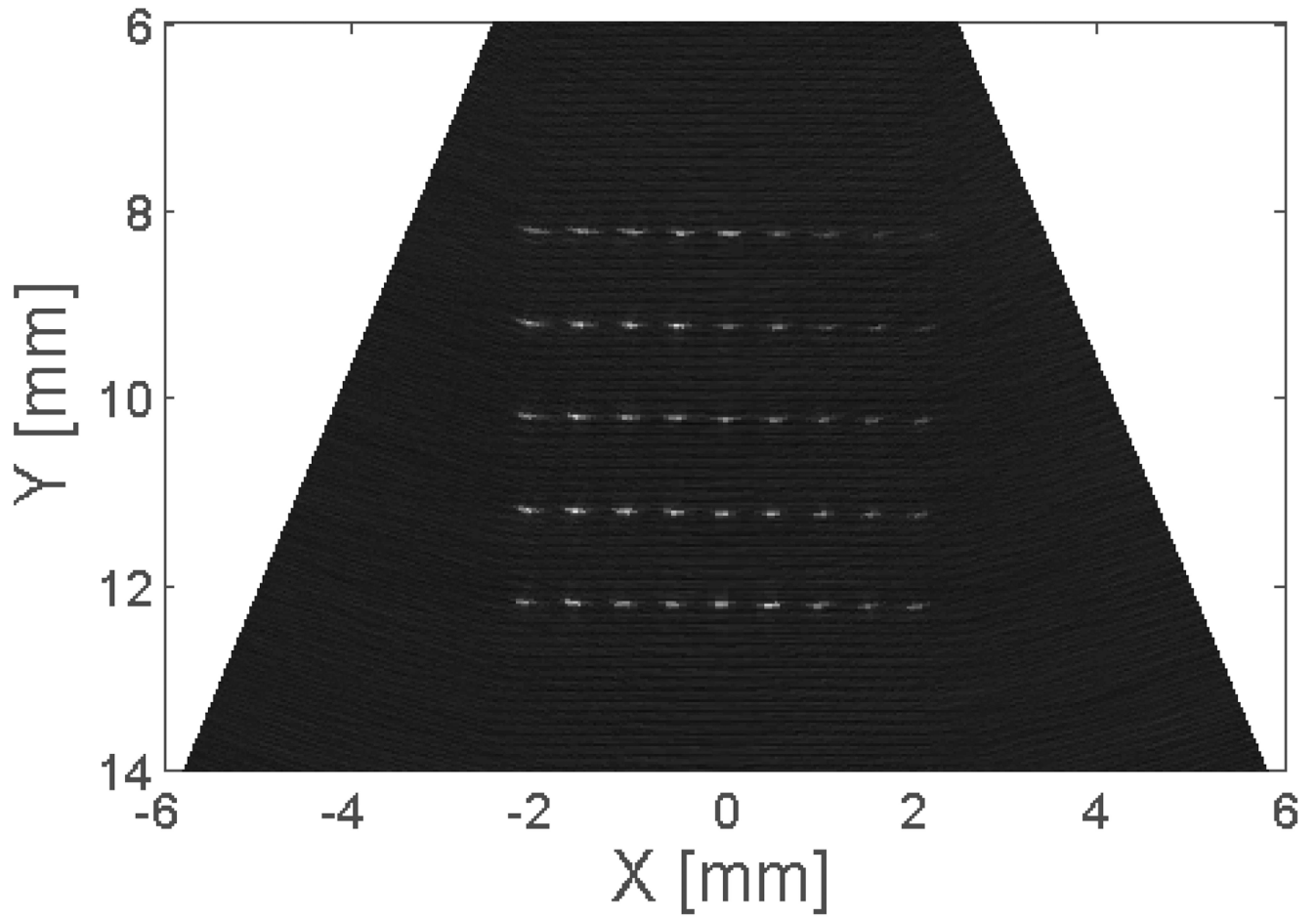
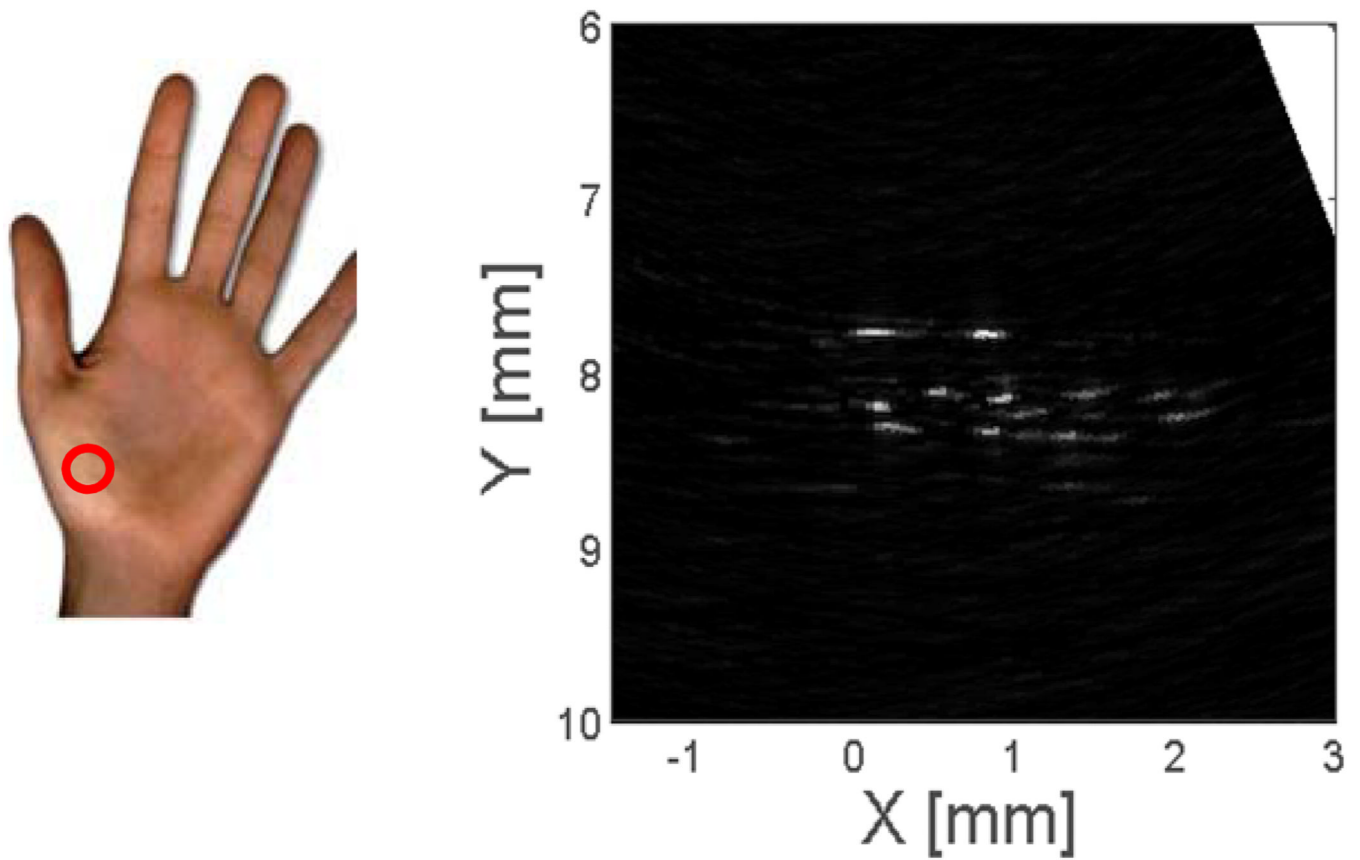


Fig. 5.  
Line spread function of PAM 6 $\mu$ m carbon fiber phantom constructed from a B-scan projected on the X-axis (distance [m]).



**Fig. 6.** PAM phantom image composite of a  $5 \times 9$  matrix of  $6\mu\text{m}$  carbon fibers in water. Image displayed with no averaging and 33dB dynamic range.



**Fig. 7.** PAM system *in vivo* image of a cross section of blood vessels in the lower portion of a human hand.

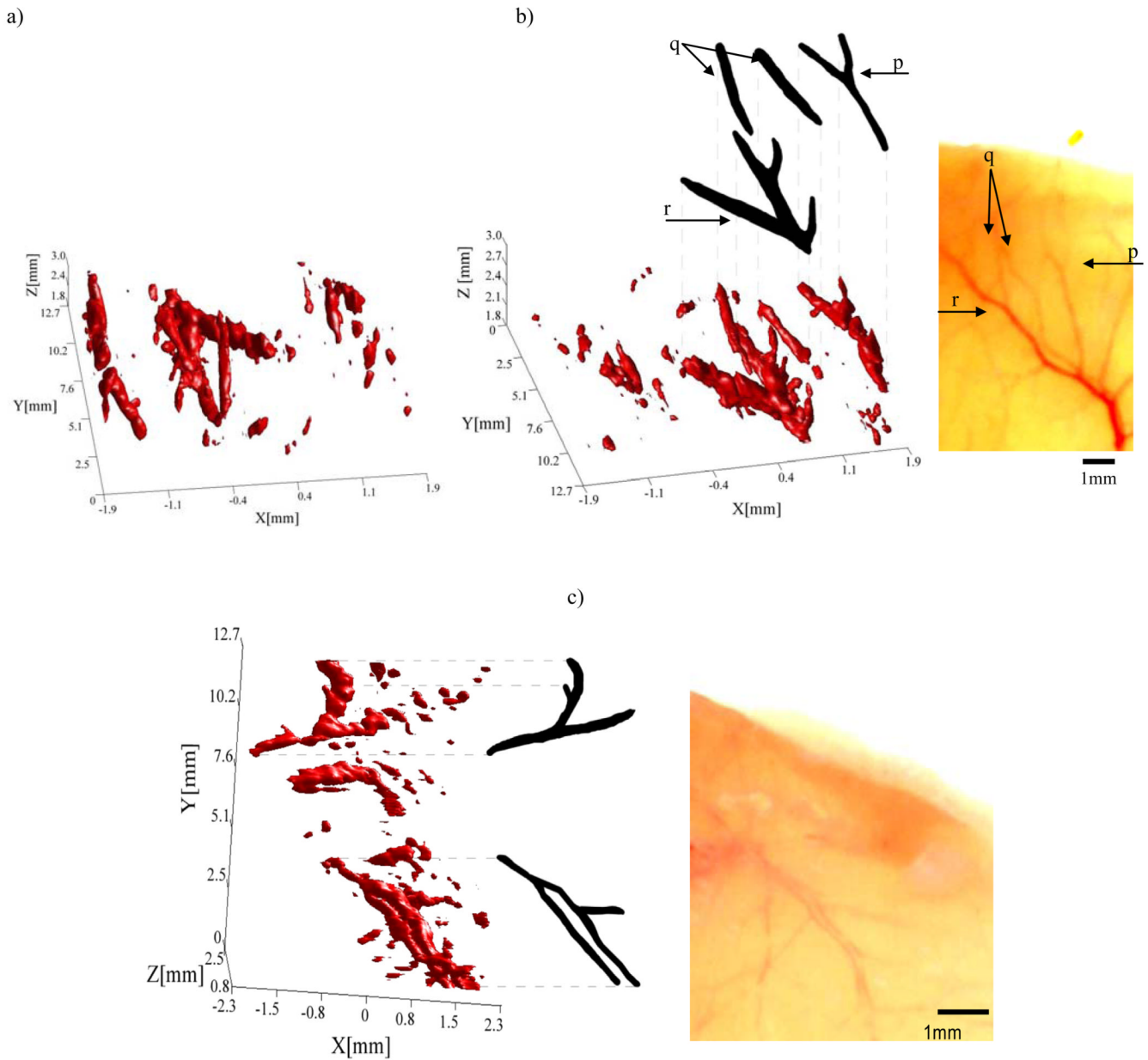


**Fig. 8.** 3D PAM images of micro-vessels below the surface of the skin in two Sprague Dawley rats graphed on axis X, Y, Z, representing lateral, scan direction, and depth dimensions, respectively. a) Rat1 PAM image showing micro-vessels with corresponding photo of excised skin b) alternate viewing angle for Rat1 image, and c) Rat2 PAM image with corresponding photo of excised skin. Markers r, p, and q denote micro-vessels within the tissue.